論文 / 著書情報
Article / Book Information

Title	Temperature change and fatigue crack initiation associated with local cyclic slip deformation in a single crystal material
Authors	Motoki Sakaguchi, Putt Thanakun, Akira Koshio, Kosuke Tokihiro, Hirotsugu Inoue
Citation	Fatigue and Fracture of Engineering Materials and Structures, Vol. 46, Issue 12, pp. 4486-4497
Pub. date	2023, 9
DOI	https://doi.org/10.1111/ffe.14146
Creative Commons	Information is in the article.

Received: 24 March 2023 | Revised: 17 August 2023 | Accepted: 20 August 2023

DOI: 10.1111/ffe.14146

ORIGINAL ARTICLE

FFEMS Fatigue & Fracture of Engineering Materials & Structures WILEY

Temperature change and fatigue crack initiation associated with local cyclic slip deformation in a single crystal material

Motoki Sakaguchi | **Putt Thanakun** | **Akira Koshio** | **Kosuke Tokihiro** | **Hirotsugu Inoue**

Department of Mechanical Engineering, Tokyo Institute of Technology, Tokyo, Japan

Correspondence
Motoki Sakaguchi, Department of Mechanical Engineering, Tokyo Institute of Technology, O-okayama 2-12-1, Meguro-ku, Tokyo 152-8552, Japan.
Email: sakaguchi.m.ac@m.titech.ac.jp

Abstract

Evaluating the fatigue limit by measuring temperature changes via infrared thermography has attracted significant interest because of its potential for rapid assessments. However, the physical background and validity of this technique are not yet fully understood. In this study, notched specimens of a single crystal Ni-base superalloy with different crystallographic orientations are subjected to cyclic loading to investigate crack initiation and temperature change. Local slip deformation is quantified using crystal plasticity finite element analyses. It is found from the experimental and analytical results that the distribution of the temperature change and the local slip deformation (a plastic shear strain on the most active slip system) are affected by the crystallographic orientation. However, the correlation between the plastic shear strain and the second harmonic amplitude, as well as the threshold values of these parameters for crack initiation, is independent of the crystallographic orientation.

KEYWORDS

crack initiation, fatigue limit, infrared thermography, single crystal, slip deformation, temperature change

Highlights

- Fatigue tests are conducted using a single crystal material.
- Crack initiation and temperature changes via infrared thermography are investigated.
- Local slip deformation is quantified using crystal plasticity finite element analyses.
- Correlations between slip deformation and temperature change are examined.

1 | INTRODUCTION

The fatigue limit is a crucial feature in structural designs. Determination of the fatigue limit by conventional fatigue testing is commonly time-consuming and costly. Therefore, since the beginning of the 20th century, methods based on temperature changes resulting from self-heating have been developed to rapidly determine the fatigue limit.[1–7] These temperatures arise from the thermoelastic effect at stresses lower than the fatigue limit and from irreversible plastic deformation at stresses above the fatigue limit.[8,9]

In the work of Geraci et al[10] and Luong,[11] an energetic approach was initially investigated to describe the self-heating mechanism correlated with energy dissipation using infrared thermography. These studies were based on experimental observations of increasing surface temperatures in materials undergoing cyclic loading. In addition, Krapez et al,[4] Bremond et al,[12] and Sakagami et al[13] used the temperature increase resulting from plastic deformation and analyzed it in the frequency domain. In this method, the double frequency component is used to evaluate the irreversible energy dissipation. This measurement method is called the 2f lock-in thermography method. Ly et al[14–16] conducted a numerical analysis to simulate the temperature change for fatigue limit evaluations considering heat conduction as well as the stress concentration effect. The evaluated results were quantitatively compared with a thermography experiment at a macroscopic scale. Even though estimations of the fatigue limit empirically coincide with the determined temperature change, the physical backgrounds and validity of the estimated fatigue properties remain unclear.

The mechanisms of energy dissipation under fatigue loading have also been investigated. Bodelot et al[17–19] simultaneously measured the strain and temperature fields at the grain scale in austenitic stainless steel under both monotonic tensile and cyclic loading using the digital image correlation technique and infrared thermography, respectively. Shiozawa et al[20] investigated the mechanism of energy dissipation concerning the formulation of slip bands in austenitic stainless steel by observing the slip bands under optical and atomic force microscopes. This study revealed that the dissipated energy corresponds to the activation of the slip band, which is based on the number of slip bands and the slip distance. Akai et al[21] performed dissipated energy measurements at a grain-size scale in austenitic stainless steel and compared them with slip band observations. They suggested that the dissipated energy is associated with the activation of the slip bands, which resulted in fatigue crack initiation. Some studies have employed crystal plasticity analysis to estimate the dissipated energy and resultant local fatigue damage by computing the resolved shear stress and the resolved shear strain on the slip system.[22,23] Wan et al[24] and Chen et al[25,26] predicted fatigue crack nucleation sites in polycrystalline materials using the stored energy calculated from the accumulated slip, stress, and geometrically necessary dislocation density. They revealed that the proposed stored energy can be used to estimate the number of cycles required for crack nucleation under different testing conditions.

Even though many studies have attempted to understand the mechanism of the dissipated energy on the fatigue behavior, these studies have employed polycrystalline materials composed of multiple grains with different crystallographic orientations. Therefore, the anisotropic cyclic deformation in each grain made it difficult to capture the correlation between the measured dissipated energy and the local slip deformation. In addition, the inhibition of slip deformation at the grain boundaries and the associated pile-up of dislocation led to complexity when correlating the temperature change with the slip deformation within the grains. Various studies have confirmed that the grain properties and crystallographic orientations of materials strongly affect the fatigue behavior and fatigue crack initiation. Primary microstructural features associated with internal crystallographic fatigue crack initiation have been identified as large grain sizes, twin boundaries, and grains with a high Schmid factor.[27]

In this study, crack initiation tests are conducted under cyclic loading both below and above the fatigue limit to investigate the temperature dissipation associated with anisotropic slip deformation. Here, a single crystal material is employed to eliminate the effect of grain boundaries, which simplifies examinations of the relationship between the in-grain temperature variation and the local fatigue damage. In addition, specimens with different crystallographic orientations are employed to study the effect of the crystallographic orientation on the temperature variation. Furthermore, the local fatigue damages are analyzed and compared using the crystal plasticity finite element (CPFE) method, which can consider the elastic anisotropy of the material and localized slip deformation.

2 | EXPERIMENTAL PROCEDURE

2.1 | Material and specimen preparation

The material employed in this study is a second-generation single crystal Ni-base superalloy, CMSX-4. The chemical composition of this material is 9.7Co–6.5Cr–6.4W–5.7Al–1.0Ti–6.6Ta–0.6Mo–3.0Re–Bal Ni [wt.%]. For this material, heat treatments were conducted as follows: solution treatments at 1277°C for 2 h, 1288°C for 2 h, 1296°C for 3 h, 1304°C for 3 h, 1313°C for 2 h, 1316°C for 2 h, and

1277°C for 2 h followed by aging treatments at 1140°C for 6 h and 871°C for 20 h.

Compact (C(T)) specimens were cut from cast ingots of CMSX-4 using wire electric discharge machining techniques. The geometry of the specimens is shown in Figure 1. The surfaces were polished with several grades of emery papers up to #2000. Buff polishing was additionally performed on one side for microscopic observations. Two types of specimens were prepared by changing the combination of the primary (loading direction) and secondary (crack propagation direction) orientations, as shown in Figure 2. Here, the first and second Miller indices for the specimens are the primary and secondary orientations, respectively. This rule for the Miller indices is identical to that in previous studies.[28–31] For example, ⟨100⟩⟨110⟩ specimen has its loading direction along the ⟨100⟩ crystallographic orientation and its crack propagation direction along the ⟨110⟩ orientation.

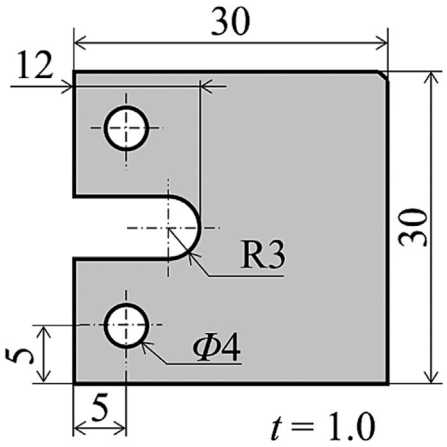

FIGURE 1 Geometry of the specimens employed in this study in [mm].

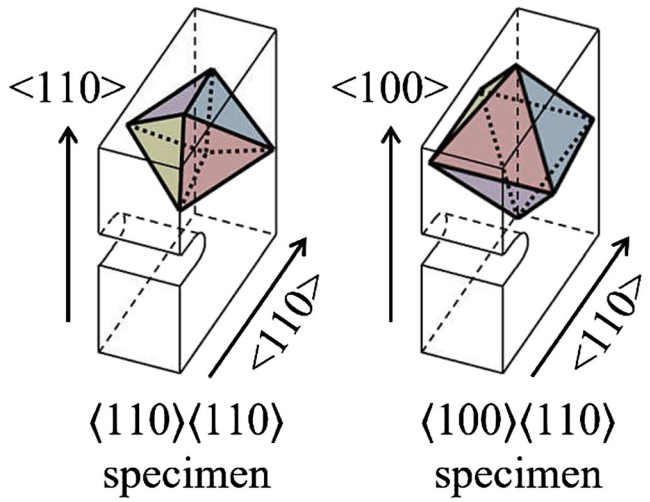

FIGURE 2 Schematic illustration of the octahedral slip planes in the two types of specimens. [Colour figure can be viewed at wileyonlinelibrary.com]

2.2 | Fatigue crack initiation tests

Fatigue crack initiation tests were conducted at room temperature using an electrohydraulic machine. During the tests, the specimen front surfaces were observed using a digital microscope (KEYENCE VHX-5000) to optically identify the slip deformation and detect crack initiation. The variation over time of the temperature on the back surfaces of the specimens was simultaneously measured using a quantum-type thermography (Cedip Infrared Systems, JADE III). Here, the back surfaces were coated by a black spray to improve the thermal emissivity. Spatial resolutions of the thermography of up to 110 μm/pixel were achieved. The frame rate of the thermography was set to 50 Hz. The test system was covered by a black sheet to block reflections from the surrounding environment.

Two different loading conditions were applied to the fatigue tests. The first fatigue test was designed to observe crack initiation when applying several different loading amplitudes to the specimens with different crystallographic orientations. These fatigue crack initiation tests were conducted by applying up to 300,000 constant-amplitude cyclic loadings to each specimen. The loading ratio and loading frequency were 0.4 and 10 Hz, respectively. A total of nine specimens were tested with loading amplitudes P_a of 150, 240, 330, 480, and 600 N for ⟨110⟩⟨110⟩ specimens and loading amplitudes of 240, 330, 480, and 600 N for ⟨100⟩⟨110⟩ specimens. During the cyclic loading, the tests were paused to observe fatigue crack initiation after a specific number of cyclic loading intervals.

The second fatigue test was conducted using a single specimen to measure the temperature changes during the cyclic loading. Tests were conducted for both ⟨110⟩⟨110⟩ and ⟨100⟩⟨110⟩ specimens with the loading amplitude P_a starting from 240 N with a loading amplitude increment of 30 N. Here, 6000 loading cycles were applied to the specimens for each loading increment. The loading ratio and loading frequency were same as in the first test. The spatial resolution of the thermography was fixed to 160 μm/pixel for this second fatigue test.

3 | EXPERIMENTAL RESULTS

3.1 | Fatigue crack initiation

Figure 3 demonstrates the relationship between the loading amplitude P_a and the number of cycles to crack initiation for each specimen. This result was obtained

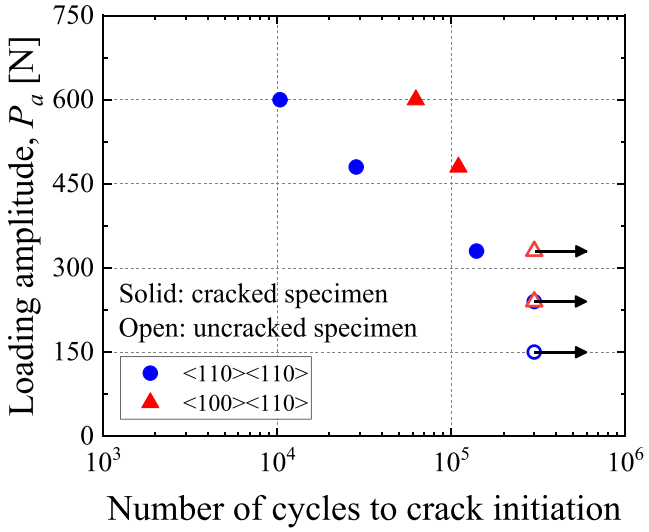

FIGURE 3 Relationship between the loading amplitude P_a and the number of cycles to crack initiation. [Colour figure can be viewed at wileyonlinelibrary.com]

from the first fatigue test applying cyclic loadings with constant amplitude. Open symbols correspond to the specimens in which no crack initiation was observed until 300,000 cycles. We see that the crack initiation cycles of ⟨110⟩⟨110⟩ specimens are shorter than those of ⟨100⟩⟨110⟩ specimens at the same P_a.

Figure 4 shows microscopic images at the notch tip for all the loading conditions in ⟨110⟩⟨110⟩ and ⟨100⟩⟨110⟩ specimens. No cracks were detected until 300,000 cycles when $P_a = 150$ N and 240 N for ⟨110⟩⟨110⟩ specimen and $P_a = 240$ N and 330 N for ⟨100⟩⟨110⟩ specimen. In the cracked specimens, the crack initiation sites differ between ⟨110⟩⟨110⟩ and ⟨100⟩⟨110⟩ specimens; that is, cracks were observed near the 0° position on the notch tip for ⟨110⟩⟨110⟩, while cracks initiated at the 30° position for ⟨100⟩⟨110⟩. These crack initiation sites, depending on the crystallographic orientations, should be determined by the strong anisotropies of the stress concentration and slip deformation in single crystal material. This is numerically discussed in Section 4 based on a crystal plasticity analysis.

3.2 | Thermography measurements

The reversible temperature change resulting from the thermoelastic effect can be observed during the cyclic loading. This temperature change T_1 can be expressed as a function of the change in the sum of the principal stresses $\Delta\sigma$ such that

$$\Delta T_1 = -\frac{\alpha}{\rho C_p} T \Delta\sigma, \tag{1}$$

where α, ρ, and C_p are the coefficient of thermal expansion, mass density, and specific heat at constant pressure, respectively. The irreversible energy dissipation, which is caused by the local plastic deformation, occurs at the maximum and minimum loadings. Here, the increase in the temperature resulting from irreversible energy dissipation occurs twice during a single loading cycle; the frequency of this temperature component is two times greater than that of the loading frequency. Accordingly, the time-series temperature change on the specimen surface measured via infrared thermography was analyzed in the frequency domain using a Fourier transformation, in which the products are called the fundamental harmonic amplitude and the second harmonic amplitude for T_1 and T_2, respectively. The experimental results for T_1 and T_2 from several loading intervals were averaged to reduce the noise from the obtained infrared thermography.

Figure 5 summarizes the distribution of the fundamental harmonic amplitude T_1 measured by infrared thermography at $P_a = 240$, 330, 480, and 600 N for ⟨110⟩⟨110⟩ and ⟨100⟩⟨110⟩ specimens. A Gaussian filter was applied to the temperature field to improve the distorted values in some pixels by considering the mean values of the surrounding pixels. Even though the absolute values of T_1 increased with the loading amplitude, the distributions are similar for all the loading conditions for both ⟨110⟩⟨110⟩ and ⟨100⟩⟨110⟩ specimens. In ⟨110⟩⟨110⟩ specimens, the maximum values of T_1 are located at $\theta = 0°$, while they are located at approximately $\theta = \pm 30°$ for ⟨100⟩⟨110⟩ specimens. Figure 6 shows the distribution of the second harmonic amplitude T_2 for ⟨110⟩⟨110⟩ and ⟨100⟩⟨110⟩ specimens measured for all the loading conditions. The distribution of T_2 becomes larger when P_a increases. This implies that the plastic deformed area becomes larger with increasing P_a.

Figure 7 plots the value of T_2 along the notch tip obtained from the second fatigue test for (a) ⟨110⟩⟨110⟩ and (b) ⟨100⟩⟨110⟩ specimens. Here, the results under the four loading amplitudes are compared. Because of the symmetry condition, only data from the upper half of the specimens are taken into consideration. The overall values of T_2 tend to increase with increasing P_a. For ⟨110⟩⟨110⟩ specimens in Figure 7A, the values of T_2 are largest at $\theta = 0°$ and decrease with the angle along the notch tip under all loading amplitudes. Conversely, for ⟨100⟩⟨110⟩ specimens in Figure 7B, the values of T_2 are largest at approximately $\theta = 30°$. Comparing ⟨110⟩⟨110⟩

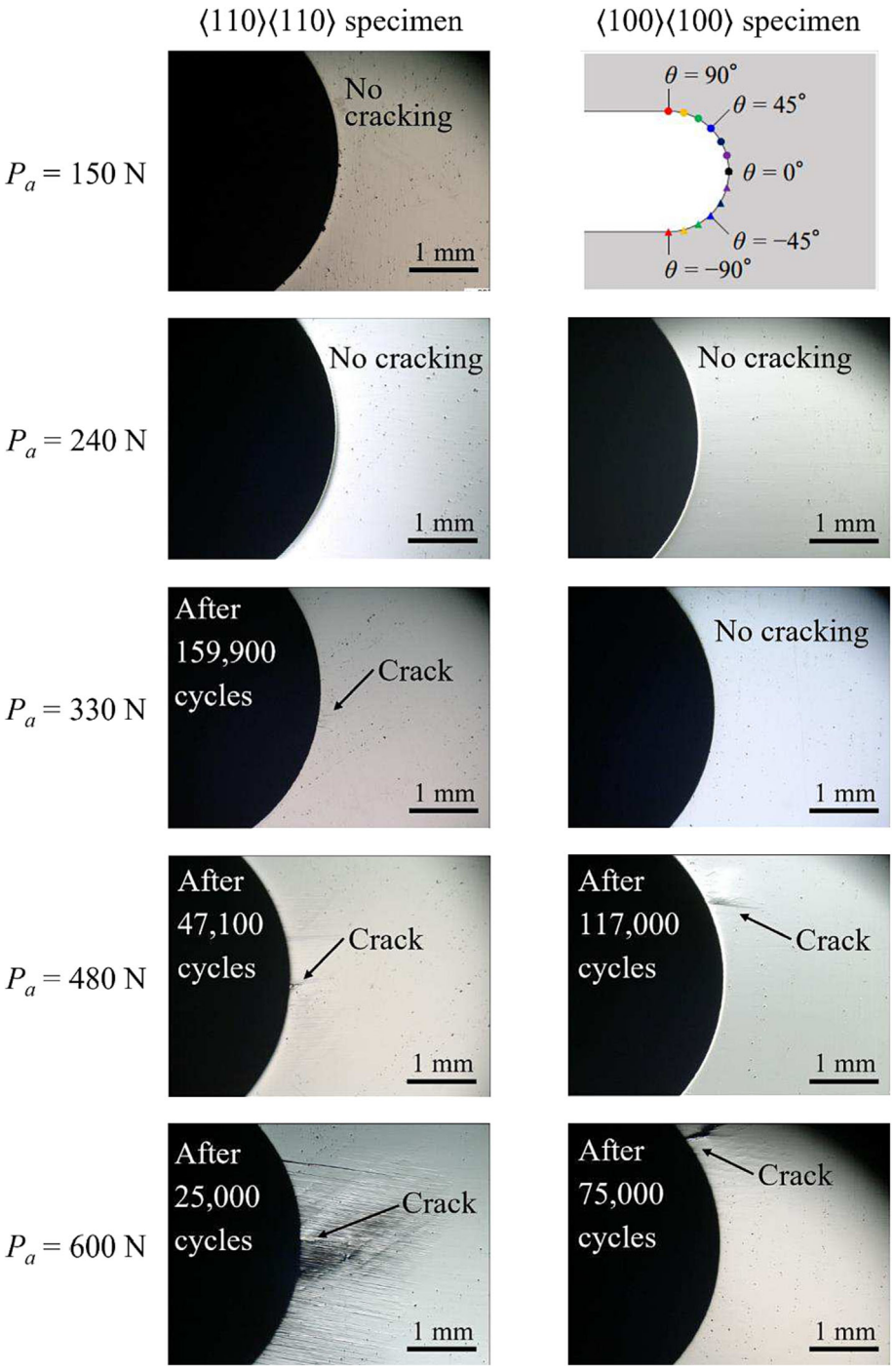

FIGURE 4 Microscopic observations at the notch tips of each type of specimen. [Colour figure can be viewed at wileyonlinelibrary.com]

and ⟨100⟩⟨110⟩ specimens, we see that the absolute values of T_2 for ⟨110⟩⟨110⟩ are higher than those for ⟨100⟩⟨110⟩ for the same loading amplitude.

Figure 8 shows the results of the second fatigue test, where the loading amplitudes were gradually increased from $P_a = 240$ N. Here, the maximum values of T_2 for two crystallographic orientations are plotted as a function of the loading amplitude. The plots corresponding to the cracked condition in the first fatigue test ($P_a \geq 330$ N for ⟨110⟩⟨110⟩ and $P_a \geq 480$ N for ⟨100⟩⟨110⟩) are represented with solid symbols and are distinguished from the uncracked loading condition, which are plotted with open symbols. The results demonstrate that the magnitude of T_2 for ⟨110⟩⟨110⟩ specimen is larger than that for ⟨100⟩⟨110⟩ specimen. This indicates that the crystallographic orientation affects the temperature change behavior during cyclic loading. Note that the value of T_2 for the cracked conditions is larger than 1.0 mK, which is common to both ⟨110⟩⟨110⟩ and ⟨100⟩⟨110⟩ specimens. This implies that the crystallographic orientation affects

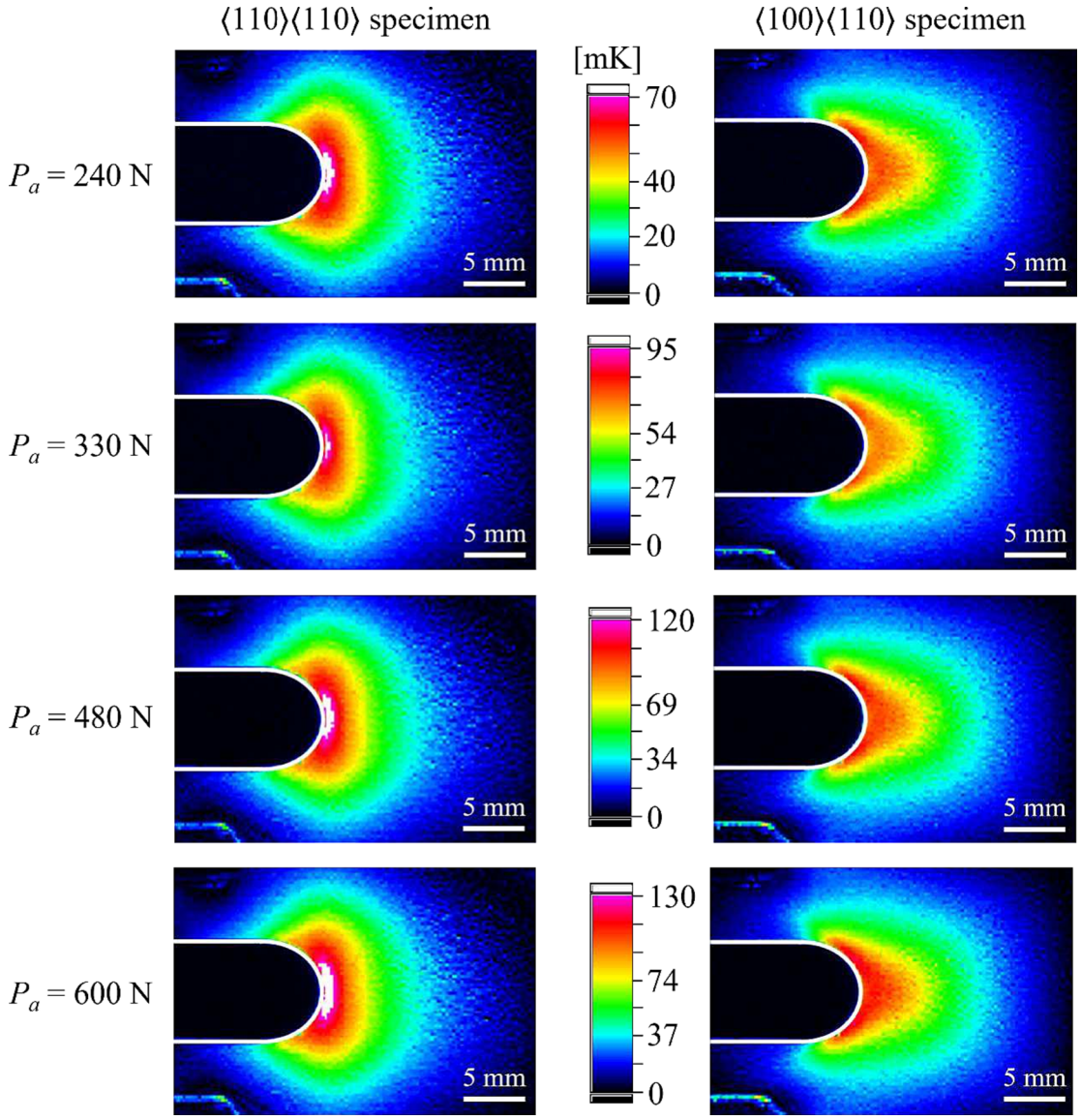

FIGURE 5 Distribution of the fundamental harmonic amplitude T_1 in ⟨110⟩⟨110⟩ and ⟨100⟩⟨110⟩ specimens. [Colour figure can be viewed at wileyonlinelibrary.com]

the temperature change but does not affect the threshold value of T_2 for fatigue crack initiation.

4 | CRYSTAL PLASTICITY ANALYSIS

The irreversible energy dissipation that occurs twice during each loading cycle, that is, T_2, is caused by local plastic deformation.[13] In face-centered cubic (FCC) materials, including the single crystal Ni-base superalloys employed in this study, the plastic deformation is primarily associated with dislocation motion along the octahedral slip system. The plastic deformation is recognized as slip, that is, a plastic shear strain along each slip system.

To precisely evaluate the anisotropic plastic deformation in a single crystal material with the aim of examining the temperature change behavior, it is preferable to quantify all the activities of the slip systems. Here, a finite element analysis incorporating the crystal plasticity theory provides the most appropriate assessment. This is because CPFE can capture the three important factors that determine the temperature change in a single crystal material: (1) the anisotropic elastic property, (2) the stress concentration around the notch tip, and (3) the anisotropic plastic deformation localized along the octahedral slip systems. The authors have previously shown that a CPFE analysis considering the actual geometry of a crystallographic crack can provide a reasonable explanation for the effect of the crystallographic orientation on

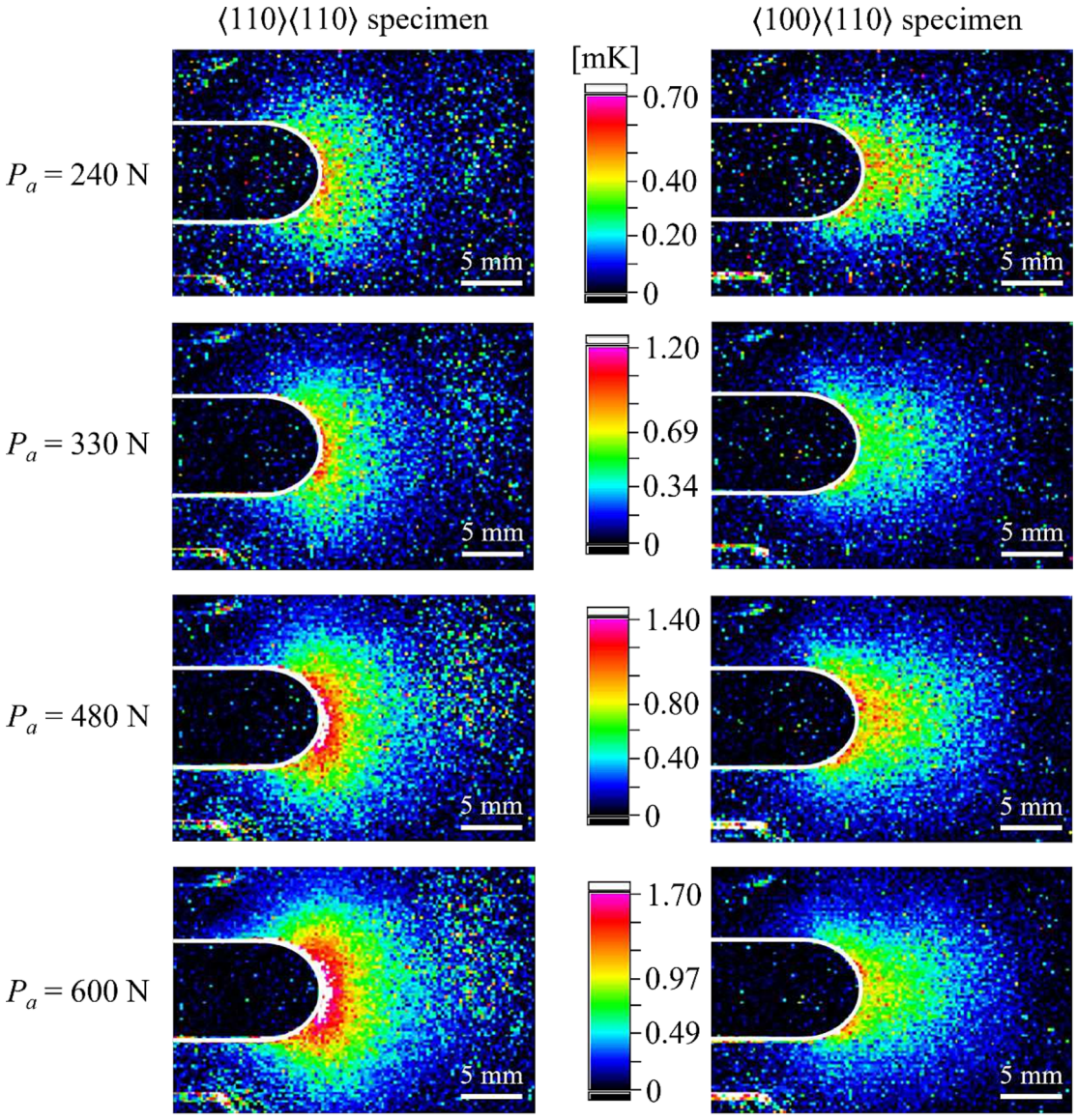

FIGURE 6 Distribution of the second harmonic amplitude T_2 in ⟨110⟩⟨110⟩ and ⟨100⟩⟨110⟩ specimens. [Colour figure can be viewed at wileyonlinelibrary.com]

the cracking path and propagation rate in a single crystal Ni-base superalloy.[28,29,31] A similar analytical framework is applied here to quantify the localized slip deformation around the notch tip.

4.1 | CPFE model

The single crystal Ni-base superalloy exhibits FCC structure that includes four types of {111} slip planes and 12 slip systems, as shown in Figure 9. Here, the blue, purple, red, and yellow slip planes represent slip planes 1, 2, 3, and 4, respectively. The slip planes and slip directions are defined in the local coordinate system, which is established with *X*-, *Y*-, and *Z*-axes in the [100], [010], and [001] directions, respectively. The global coordinate system, which is kept the same under the different crystallographic orientations, is the reference for the rotation of the defined local coordinate system. Here, the *X*-, *Y*-, and *Z*-axes are defined to be the crack propagation, loading, and thickness directions, respectively. The crystallographic orientations can be obtained by rotating the crystal in the global coordinate system in the local coordinate system. ⟨100⟩⟨110⟩ specimen can be obtained by rotating the crystal around the *Y*-axis by −45°, and ⟨110⟩⟨110⟩ specimen can be obtained by rotating around the *Z*-axis by 45° in the global coordinate system.

The crystal plasticity theory employed in this study is based on the theoretical framework of Asaro.[32] The constitutive equation is given as follows:

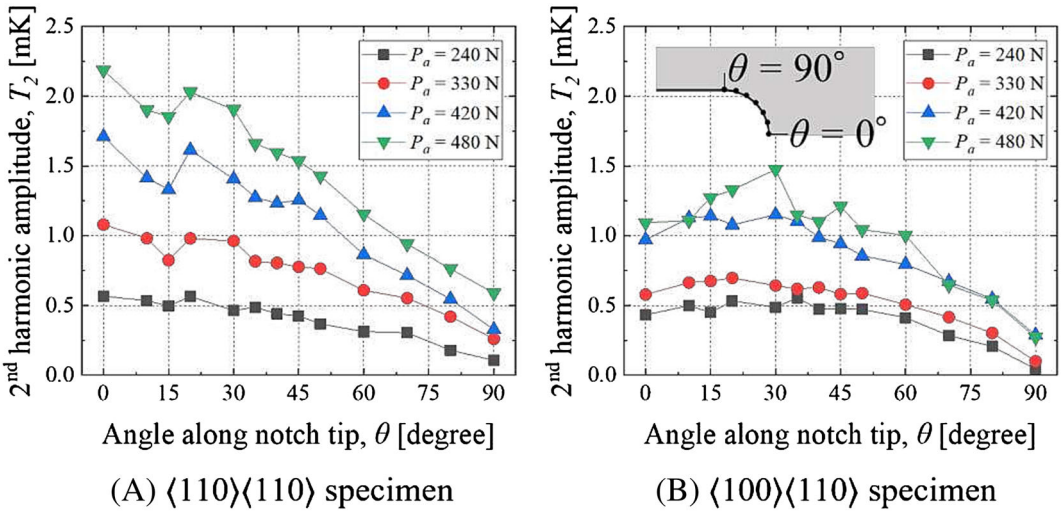

FIGURE 7 Relationship between the measured T_2 and loading amplitude P_a along the notch tip of (A) ⟨110⟩⟨110⟩ and (B) ⟨100⟩⟨110⟩ specimens obtained from the second fatigue test. [Colour figure can be viewed at wileyonlinelibrary.com]

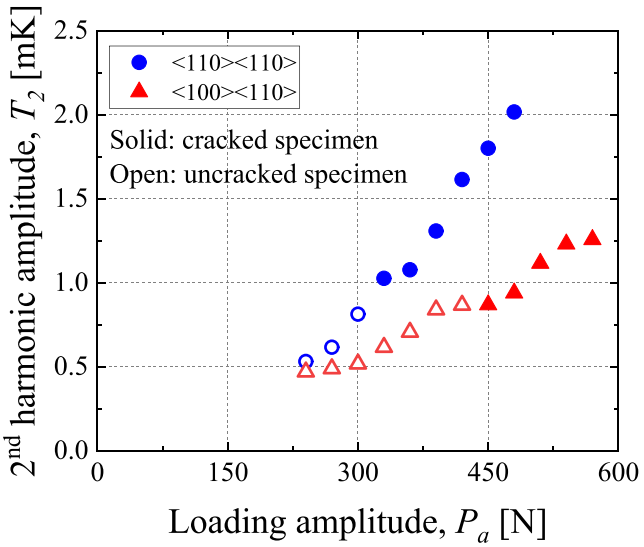

FIGURE 8 Relationship between the maximum value of T_2 and the loading amplitude P_a for ⟨110⟩⟨110⟩ and ⟨100⟩⟨110⟩ specimens obtained from the second fatigue test. [Colour figure can be viewed at wileyonlinelibrary.com]

$$\nabla\sigma = \mathbf{C}:\mathbf{D} - \sum_{k=1}^{n}\left(\mathbf{C}:\mathbf{P}^{k} + \mathbf{W}^{k}\bullet\sigma - \sigma\bullet\mathbf{W}^{k}\right)\dot{\gamma}^{k}. \quad (2)$$

Here, $\nabla\sigma$ is the Jaumann rate of the Cauchy stress, σ is the stress, $\mathbf{C}$ is a tensor of the elastic moduli, and $\mathbf{D}$ is the deformation rate tensor. $\mathbf{P}^{k}$ and $\mathbf{W}^{k}$ are the stretching and spin tensors, respectively, for a slip system k such that

$$\mathbf{P}^{k} = \frac{1}{2}\left(\mathbf{n}^{k}\otimes\mathbf{b}^{k} + \mathbf{b}^{k}\otimes\mathbf{n}^{k}\right), \quad (3)$$

$$\mathbf{W}^{k} = \frac{1}{2}\left(\mathbf{n}^{k}\otimes\mathbf{b}^{k} - \mathbf{b}^{k}\otimes\mathbf{n}^{k}\right). \quad (4)$$

Here, $\mathbf{n}^{k}$ and $\mathbf{b}^{k}$ are the unit direction vectors of the slip plane normal and slip direction, respectively. $\dot{\gamma}^{k}$ in Equation (3) is the shear strain rate of a slip system k, as given in the following kinetic law:

$$\dot{\gamma}^{k} = \dot{\gamma}_0\,\mathrm{sgn}\left(\frac{\tau^{k}}{\tau_0}\right)\left|\frac{\tau^{k}}{\tau_0}\right|^{1/m}. \quad (5)$$

Here, τ^{k} is the resolved shear stress along the slip system k; $\dot{\gamma}_0$ and τ_0 are the reference shear strain rate and the yield shear stress, respectively; and m is a rate-dependent parameter. These constitutive equations are incorporated in Abaqus for an implicit analysis with a user-defined material subroutine UMAT for single crystal plasticity. The material parameters m, τ_0, and $\dot{\gamma}_0$ were set to $m = 0.01$, $\tau_0 = 360$ MPa, and $\dot{\gamma}_0 = 1\times10^{-5}$ to reproduce the stress–strain relationship in the tensile test at room temperature. Because the single crystal Ni-base superalloy shows elastic–perfectly plastic behavior at room temperature,[33] strain hardenings of the slip systems were not considered.

Finite element models were established by following the specimen geometry shown in Figure 1. Because of the symmetry condition, only a quarter of a specimen was modeled to optimize the time and cost of the analysis. The numbers of elements and nodes in the models were approximately 100,000 and 475,000, respectively. The minimum mesh size in the vicinity of the notch tip was 10 μm, which was confirmed to be sufficiently fine for

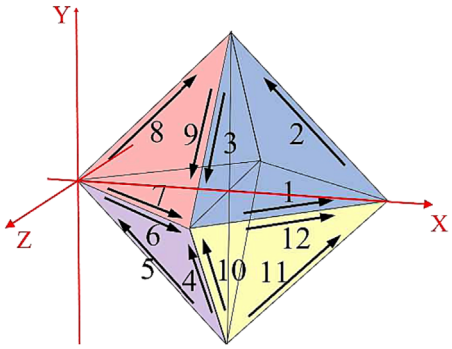

Slip systems	Slip planes	Slip directions
1	Plane 1: (111)	$[\bar{1}01]$
2		$[\bar{1}10]$
3		$[0\bar{1}1]$
4	Plane 2: $(\bar{1}\bar{1}1)$	$[011]$
5		$[\bar{1}10]$
6		$[101]$
7	Plane 3: $(\bar{1}11)$	$[101]$
8		$[110]$
9		$[0\bar{1}1]$
10	Plane 4: $(1\bar{1}1)$	$[011]$
11		$[110]$
12		$[\bar{1}01]$

FIGURE 9 Slip planes and slip systems in a face-centered cubic structure. [Colour figure can be viewed at wileyonlinelibrary.com]

stable calculations based on convergence and sensitivity studies. The element type was C3D20R to ensure the high precision of the calculation results. An external load was applied by a point force to the reference point at the center of the loading hole, simulating the maximum load in the experiments. The displacement in the horizontal direction of this reference point was constrained, and the distance between the reference point and the upper half surface of the loading hole was kept constant to allow rotation of the specimen during loading. The anisotropic elastic moduli for CMSX-4 at room temperature were set to $C_{11} = 248.8$ GPa, $C_{12} = 158.5$ GPa, and $C_{44} = 129.8$ GPa according to Siebörger et al.[34] The crystallographic orientation was defined by setting the axis directions of the global and local coordinate systems.

4.2 | Numerical results of the CPFE analysis

4.2.1 | Fundamental harmonic amplitude T_1

Figure 10 shows the sum of the principal stresses $\Delta\sigma$ obtained from the CPFE analysis for $\langle 110\rangle\langle 110\rangle$ and $\langle 100\rangle\langle 110\rangle$ models. Here, the distribution at $P_a = 480$ N was chosen for the comparison, where crack initiation can be observed in both specimens. Comparing the computed contours of $\Delta\sigma$ with the measured temperature distribution T_1 shown in Figure 5, the distributions of $\Delta\sigma$ are clearly similar to those of T_1 for each crystallographic orientation. For $\langle 110\rangle\langle 110\rangle$ model, the computed $\Delta\sigma$ (Figure 10A) and measured T_1 (Figure 5) are both highest at $\theta = 0°$. Conversely, these parameters are dominant at approximate $\theta = \pm 35°$ in $\langle 100\rangle\langle 110\rangle$ model. This shows that the CPFE analysis can simulate the anisotropic stress distributions in this study around the notch tip.

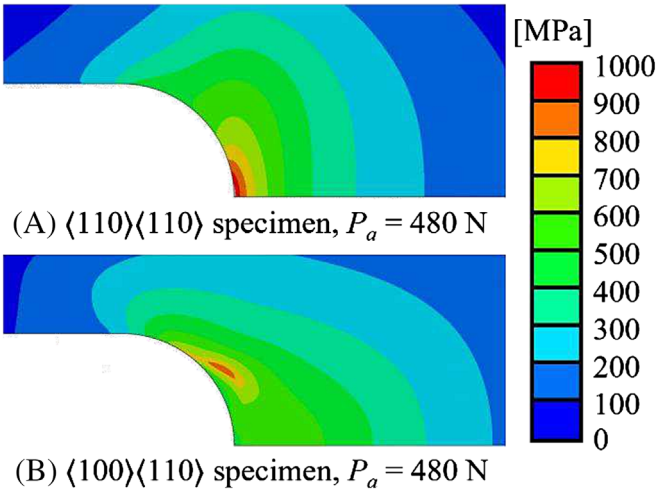

FIGURE 10 Contours of the change in the sum of the principal stresses where $P_a = 480$ N for (A) $\langle 110\rangle\langle 110\rangle$ and (B) $\langle 100\rangle\langle 110\rangle$ models. [Colour figure can be viewed at wileyonlinelibrary.com]

4.2.2 | Second harmonic amplitude T_2

Figure 11 shows the distribution of the plastic shear strain obtained from the CPFE analysis for (a) $\langle 110\rangle\langle 110\rangle$ and (b) $\langle 100\rangle\langle 110\rangle$ models where $P_a = 480$ N. The most dominant plastic shear strains in the 12 slip systems are represented, because crack initiations should be controlled by the most active slip system according to the critical plane approach.[35] The octahedral slip planes are given at the bottom left of each figure to indicate the dominant slip system in a similar perspective viewing direction to the finite element model. Here, the dominant plastic shear strains in $\langle 110\rangle\langle 110\rangle$ and $\langle 100\rangle\langle 110\rangle$ models are along slip system numbers 3 and 10, respectively. The plastic shear strain is concentrated around the $\theta = 0°$

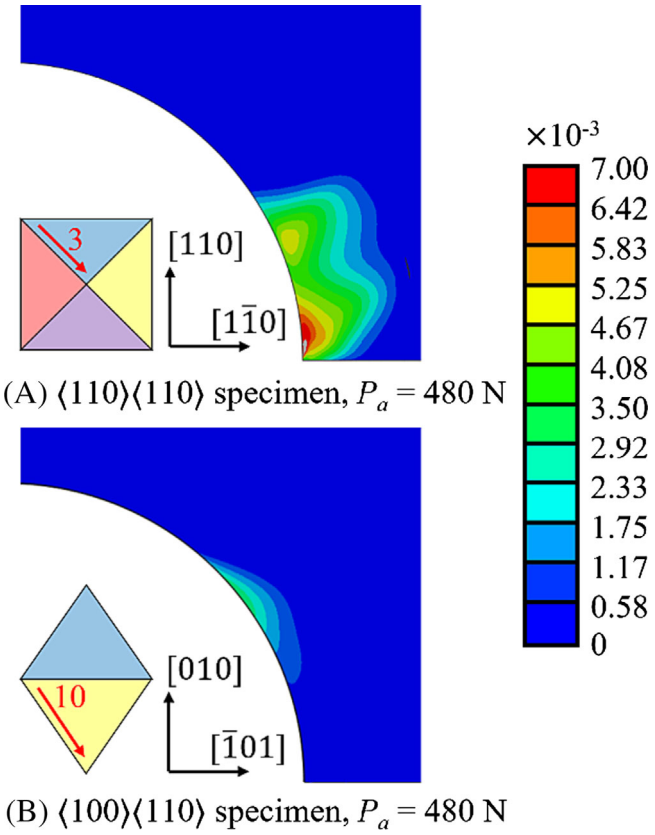

FIGURE 11 Contours of the plastic shear strain on the most active slip system where $P_a = 480$ N for (A) ⟨110⟩⟨110⟩ and (B) ⟨100⟩⟨110⟩ specimens. [Colour figure can be viewed at wileyonlinelibrary.com]

and $\theta = 35°$ positions in ⟨110⟩⟨110⟩ and ⟨100⟩⟨110⟩ models, respectively. The locations of the highest plastic shear strain correspond to the experimental observations in Figure 4, where cracks were initiated at approximately $\theta = 0°$ and $\theta = 30°$ in ⟨110⟩⟨110⟩ and ⟨100⟩⟨110⟩ specimens, respectively. In addition, the computed contours of the plastic shear strain in both models are similar to the T_2 distribution, even though the generated contour in ⟨110⟩⟨110⟩ model had a slightly different configuration. This result is thought to be due to the heat conduction effect in the specimen, which is not considered in this study.

Figure 12 shows the distribution of the plastic shear strain γ_{max} along the most active slip systems as a function of the angle along the notch tip θ. Here, the computed results for $P_a = 330$ N and 480 N are plotted for ⟨110⟩⟨110⟩ model, while the result for $P_a = 480$ N is shown for ⟨100⟩⟨110⟩ model, with the plastic shear strain under $P_a = 330$ N being relatively lower. In Figure 12, the highest plastic shear strain is generated near $\theta = 0°$ in ⟨110⟩⟨110⟩ model under both P_a conditions, while it is near $\theta = 35°$ in ⟨100⟩⟨110⟩ model. For ⟨110⟩⟨110⟩ model,

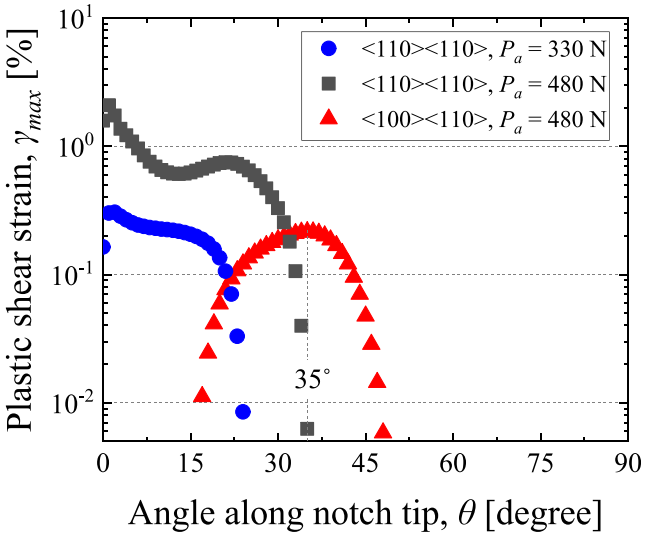

FIGURE 12 Relationship between the plastic shear strain on the most active slip system and the angle along the notch tip. [Colour figure can be viewed at wileyonlinelibrary.com]

the computed value of γ_{max} under $P_a = 480$ N is 10 times larger than that under $P_a = 330$ N. Comparing the two sets of data at $P_a = 480$ N for the two models, the values of the plastic shear strain significantly differ, with the plastic shear strain being larger in ⟨110⟩⟨110⟩ model under the same loading amplitude. This result indicates that the crystallographic orientation strongly affects the magnitude and distribution of the anisotropic plastic deformation around the notch tip. The highest values of γ_{max} in ⟨110⟩⟨110⟩ model under $P_a = 330$ N and ⟨100⟩⟨110⟩ model under $P_a = 480$ N are nearly comparable at approximately $\gamma_{max} = 0.3\%$, even though the locations of these maximum values are different. Note that the crack initiation lives under these two conditions are comparable, namely, 159,900 cycles and 117,000 cycles for ⟨110⟩⟨110⟩ specimen under $P_a = 330$ N and ⟨100⟩⟨110⟩ specimen under $P_a = 480$ N, respectively.

Figure 13 shows the relationship between the second harmonic amplitude T_2 and the maximum values of γ_{max} along the most active slip system for each loading amplitude. The data plots are distinguished by solid and open symbols for the cracked and uncracked specimens, respectively. The values of γ_{max} in both ⟨110⟩⟨110⟩ and ⟨100⟩⟨110⟩ models increase with the measured values of T_2. Note in Figure 13 that the plots between T_2 and γ_{max} for both specimens align in a single trendline, while the T_2 values for the two specimens are different when they are plotted as a function of the loading amplitude, as shown in Figure 8. The threshold value of T_2 for crack initiation was approximately 1 mK for both ⟨110⟩⟨110⟩ and ⟨100⟩⟨110⟩ specimens, as in Figure 8. The corresponding value of γ_{max} for this threshold is

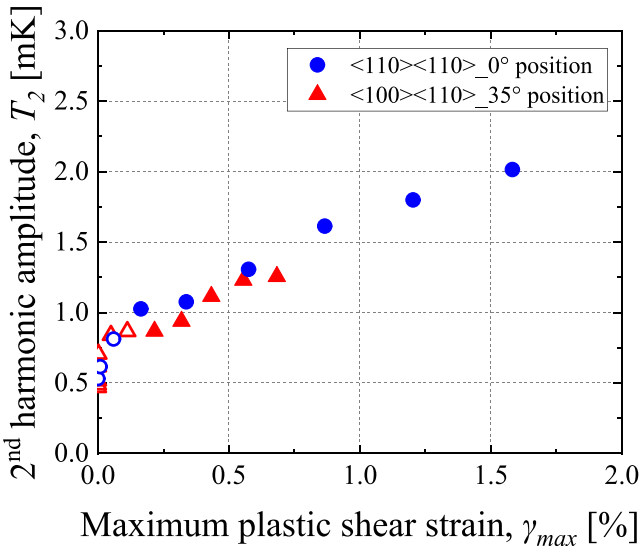

FIGURE 13 Relationship between the maximum value of the plastic shear strain for each loading amplitude and T_2 at the corresponding location. [Colour figure can be viewed at wileyonlinelibrary.com]

approximately 0.15% for both models. This indicates that the threshold value for crack initiation is independent of the crystallographic orientation when evaluating based on γ_{max} as well as T_2. The intercept value of the T_2 axis in Figure 13, approximately 0.7 mK, is presumed to be due to the thermoelastic effect and the noise of the testing system, which should be further investigated to clearly understand the temperature change mechanisms during cyclic loading. The gradient between T_2 and γ_{max} in Figure 13 also needs to be quantified, considering the micro-mechanisms of slip deformation associated with dislocation motion, the relevant energy dissipation, and the effect of heat conduction.

5 | CONCLUSIONS

To examine the in-grain temperature change and the fatigue crack initiation during cyclic loading, fatigue tests were conducted on a single-crystal material to eliminate the effect of grain boundaries. The conclusions can be summarized as follows.

1. Fatigue tests were conducted on two types of specimens with different crystallographic orientations. The location of crack initiation, number of cycles to crack initiation, and magnitude of the temperature change were different for these specimens.
2. Crystal plasticity finite element analyses were conducted to investigate the plastic deformation, namely, the slip, of an octahedral slip system near the notch tip. The plastic shear strain on the most active slip system can rationalize the temperature change with respect to the crystallographic orientation.
3. The distribution of the plastic shear strain and second harmonic amplitude are affected by the crystallographic orientation. However, the correlation between the plastic shear strain and the second harmonic amplitude, as well as the threshold values of these two parameters at the fatigue limit, is independent of the crystallographic orientations.

AUTHOR CONTRIBUTIONS

Motoki Sakaguchi: Conceptualization, supervision, funding, and writing—review and editing. **Putt Thanakun:** Formal analysis and writing—original draft. **Akira Koshio:** Conducting experiment and methodology. **Kosuke Tokihiro:** Conducting experiment and methodology. **Hirotsugu Inoue:** Supervision, funding.

ACKNOWLEDGMENT

We thank Martha Evonuk, PhD, from Edanz (https://jp.edanz.com/ac), for editing a draft of this manuscript.

CONFLICT OF INTEREST STATEMENT

The authors declare that they have no known competing financial interests or personal relationships that could have appeared to influence the work reported in this paper.

DATA AVAILABILITY STATEMENT

The data in this paper are available from the corresponding author upon reasonable request.

ORCID

Motoki Sakaguchi https://orcid.org/0000-0003-2862-4731

Hirotsugu Inoue https://orcid.org/0000-0003-0554-7710

REFERENCES

1. Stromeyer CE. The determination of fatigue limits under alternating stress conditions. *Proc Math Phys Eng Sci*. 1914;90:411-425.
2. Luong MP. Fatigue limit evaluation of metals using an infrared thermographic technique. *Mech Mater*. 1998;28(1-4):155-163.
3. La Rosa G, Risitano A. Thermographic methodology for rapid determination of the fatigue limit of materials and mechanical components. *Int J Fatigue*. 2000;22(1):65-73.
4. Krapez J-C, Pacou D, Gardette G. Lock-in thermography and fatigue limit of metals. In: *5th Conference on Quantitative Infrared Thermography*. 2000.
5. De Finis R, Palumbo D, Ancona F, Galietti U. Fatigue limit evaluation of various martensitic stainless steels with new robust thermographic data analysis. *Int J Fatigue*. 2015;74:88-96.

6. Kawai R, Yoshikawa T, Kurokawa Y, Irie Y, Inoue H. Rapid evaluation of fatigue limit using infrared thermography: comparison between two methods for quantifying temperature evolution. *Mech Eng J*. 2017;4(5):1-11.
7. Palumbo D, De Finis R, Di Carolo F, Vasco-Olmo J, Diaz FA, Galietti U. Influence of second-order effects on thermoelastic behaviour in the proximity of crack tips on titanium. *Exp Mech*. 2022;62(3):521-535.
8. Curà F, Gallinatti AE, Sesana R. Dissipative aspects in thermographic methods. *Fatigue Fract Eng Mater Struct*. 2012;35(12):1133-1147.
9. Maquin F, Pierron F. Heat dissipation measurements in low stress cyclic loading of metallic materials: from internal friction to micro-plasticity. *Mech Mater*. 2009;41(8):928-942.
10. Geraci AL, La Rosa G, Risitano A, Grech M. Determination of the fatigue limit of an austempered ductile iron using thermal infrared imagery. *Proc SPIE*. 1995;2646:306-317.
11. Luong MP. Infrared thermography of fatigue in metals. *Proc SPIE*. 1992;1682:222-233.
12. Bremond P, Potet P. Lock-in thermography: a tool to analyse and locate thermo-mechanical mechanisms in materials and structures. *Proc SPIE*. 2001;4360:560-566.
13. Sakagami T, Kubo S, Tamura E, Nishimura T. Identification of plastic-zone based on double frequency lock-in thermographic temperature measurement. In: *11th International Conference on Fracture 2005, ICF11*. 2005.
14. Ly HA, Inoue H, Irie Y. Numerical simulation on rapid evaluation of fatigue limit through temperature evolution. *J Solid Mech Mater Eng*. 2011;5(9):459-475.
15. Ly HA, Inoue H, Irie Y. Numerical study on stress concentration effect in rapid evaluation of fatigue limit through temperature evolution. *J Solid Mech Mater Eng*. 2012;6(4):299-313.
16. Ly HA, Inoue H. Effect of heat conduction on rapid evaluation of fatigue limit based on temperature evolution due to cyclic loading. *Mech Eng J*. 2019;6(3):18-00451.
17. Bodelot L, Sabatier L, Charkaluk E, Dufrénoy P. Experimental setup for fully coupled kinematic and thermal measurements at the microstructure scale of an AISI 316L steel. *Mater Sci Eng a*. 2009;501(1-2):52-60.
18. Bodelot L, Sabatier L, Charkaluk E, Dufrénoy P. Experimental determination of fully-coupled kinematical and thermal fields at the scale of grains under cyclic loading. *Adv Eng Mater*. 2009;11(9):723-726.
19. Bodelot L, Charkaluk E, Sabatier L, Dufrénoy P. Experimental study of heterogeneities in strain and temperature fields at the microstructural level of polycrystalline metals through fully-coupled full-field measurements by digital image correlation and infrared thermography. *Mech Mater*. 2011;43(11):654-670.
20. Shiozawa D, Inaba K, Akai A, Sakagami T. Experimental study of relationship between energy dissipation and fatigue damage from observation of slip band by atomic force microscope. *Adv Mat Res*. 2014;891–892:606-611.
21. Akai A, Shiozawa D, Yamada T, Sakagami T. Energy dissipation measurement in improved spatial resolution under fatigue loading. *Exp Mech*. 2020;60(2):181-189.
22. Naderi M, Amiri M, Iyyer N, Kang P, Phan N. Prediction of fatigue crack nucleation life in polycrystalline AA7075-T651 using energy approach. *Fatigue Fract Eng Mater Struct*. 2016;39(2):167-179.
23. Khan R, Alfozan A. Modeling of twinning-induced plasticity using crystal plasticity and thermodynamic framework. *Acta Mech*. 2019;230(8):2687-2715.
24. Wan VVC, Maclachlan DW, Dunne FPE. A stored energy criterion for fatigue crack nucleation in polycrystals. *Int J Fatigue*. 2014;68:90-102.
25. Chen B, Jiang J, Dunne FPE. Microstructurally-sensitive fatigue crack nucleation in Ni-based single and oligo crystals. *J Mech Phys Solids*. 2017;106:15-33.
26. Chen B, Jiang J, Dunne FPE. Is stored energy density the primary meso-scale mechanistic driver for fatigue crack nucleation? *Int J Plast*. 2018;101:213-229.
27. Miao J, Pollock TM, Wayne JJ. Crystallographic fatigue crack initiation in nickel-based superalloy René 88DT at elevated temperature. *Acta Mater*. 2009;57(20):5964-5974.
28. Chen X, Sakaguchi M. Transition behavior from mode I cracking to crystallographic cracking in a Ni-base single crystal superalloy. *Int J Fatigue*. 2020;132:105400.
29. Chen X, Hu D, Sakaguchi M. Temperature dependent transition from mode I to crystallographic cracking in a Ni-base single crystal superalloy. *Theor Appl Fract Mech*. 2023;124:103795.
30. Suzuki S, Sakaguchi M, Inoue H. Temperature dependent fatigue crack propagation in a single crystal Ni-base superalloy affected by primary and secondary orientations. *Mater Sci Eng a*. 2018;724:559-565.
31. Sakaguchi M, Komamura R, Chen X, Higaki M, Inoue H. Crystal plasticity assessment of crystallographic stage I crack propagation in a Ni-based single crystal superalloy. *Int J Fatigue*. 2019;123:10-21.
32. Asaro RJ. Crystal plasticity. *J Appl Mech*. 1983;50:921-934.
33. Zhang H, Li P, Gong X, et al. Tensile properties, strain rate sensitivity and failure mechanism of single crystal superalloys CMSX-4. *Mater Sci Eng a*. 2020;782:139105.
34. Siebörger D, Knake H, Glatzel U. Temperature dependence of the elastic moduli of the nickel-base superalloy CMSX-4 and its isolated phases. *Mater Sci Eng a*. 2001;298(1-2):26-33.
35. Fatemi A, Socie DF. A critical plane approach to multiaxial fatigue damage including out-of-phase loading. *Fatigue Fract Eng Mater Struct*. 1988;11(3):149-165.

How to cite this article: Sakaguchi M, Thanakun P, Koshio A, Tokihiro K, Inoue H. Temperature change and fatigue crack initiation associated with local cyclic slip deformation in a single crystal material. *Fatigue Fract Eng Mater Struct*. 2023;e14146. doi:10.1111/ffe.14146